A computational model for assessing impact of interfacial morphology on polymer electrolyte fuel cell performance

Hemant Bajpai, Manish Khandelwal[1], E.C. Kumbur[2], M.M. Mench[*]

Fuel Cell Dynamics and Diagnostics Laboratory, Department of Mechanical and Nuclear Engineering, The Pennsylvania State University, University Park, PA 16802, USA

ABSTRACT

A two-dimensional, non-isothermal, anisotropic numerical model is developed to investigate the impact of the interfacial morphology between the micro-porous layer (MPL) and the catalyst layer (CL) on the polymer electrolyte fuel cell (PEFC) performance. The novel feature of the model is the inclusion of directly measured surface morphological information of the MPL and the CL. The interfacial morphology of the MPL and the CL was experimentally characterized and integrated into the computational framework, as a discrete interfacial layer. To estimate the impact of MPL|CL interfacial surface morphology on local ohmic, thermal and mass transport losses, two different model schemes, one with the interface layer and one with the traditionally used perfect contact are compared. The results show a ∼54 mV decrease in the performance of the cell due to the addition of interface layer at 1 A cm^{-2}. Local voids present at the MPL|CL interface are found to increase ohmic losses by ∼37 mV. In-plane conductivity adjacent to the interface layer is determined to be the key controlling parameter which governs this additional interfacial ohmic loss. When the interfacial voids are simulated to be filled with liquid water, the overpotential on the cathode side is observed to increase by ∼25 mV. Local temperature variation of up to 1 °C is also observed at the region of contact between the MPL and the CL, but has little impact on predicted voltage.

© 2010 Elsevier B.V. All rights reserved.

1. Introduction

Improvements in cost and durability are required to achieve a large-scale commercialization of polymer electrolyte fuel cells (PEFCs). In order to achieve these improvements, a deeper understanding of local phenomena occurring inside the cell and its components are of vital importance.

Specifically, an optimal heat and water balance must be maintained [1–4]. This involves balancing the operation to avoid flooding while maintaining membrane hydration. A major unresolved question in the science of water management is the general inability for computational models to accurately predict the observed water distribution and limiting current density. This is likely due to a variety of reasons. One major bottleneck is the lack of fundamental understanding and treatment of the true interfacial contact region between the rough micro-porous layer (MPL) and catalyst layer (CL) surfaces, which is typically treated as infinitely thin with perfect contact. Recent work [5–8] at the Pennsylvania Fuel Cell Dynamics and Diagnostics Lab (FCDDL) has shown considerable interfacial gaps can exist even under compression and can store up to 6–18% of total water content in PEFC under normal operating condition. A study by Hartnig et al. using sectional X-ray radiography demonstrated significant accumulation of water at interfaces in the PEFC [9].

Among the various interfaces, the MPL|CL interface is of particular importance because of its common border with reaction sites of the catalyst layer. The main source of potential heat and water management issues associated with the MPL|CL interface originates from the imperfect mating of MPL and CL, which can cause significant interfacial gaps and increase the thermal and electrical contact resistance. These voids can also act as the water pooling locations due to low local capillary pressure. This could play a crucial role in blocking the reactant gas transport. Therefore, it is necessary to investigate the role of the MPL|CL interface using realistic contact region to investigate its role in ohmic, heat and mass transport issues.

Despite the hundreds of published models in PEFC literature, there are only few [13–18] that consider interfacial effects. Most recently, Mench and co-workers at FCDDL have shown the existence of interfacial gaps and its effect on cell resistance [10–12]. These interfacial resistances can be exacerbated by PEFC operating conditions, especially during sub-zero environment. Nitta and co-workers [13,14] considered the diffusion media (DM) and the

---

Nomenclature

C	Concentration
D	Diffusivity
T	Temperature
k	Thermal conductivity
I	Current
P	Pressure
F	Faraday constant
R	Universal gas constant
a	Water activity
U	Open circuit voltage
ΔS	Change in entropy

Subscripts

x	Through-plane direction
y	In-plane direction
e	Ionic
s	Electronic
oc	Open circuit
i	Species index
w	Water
a	Anode
c	Cathode

Greek letters

φ	Voltage
κ	Ionic conductivity
σ	Electronic conductivity
α	Transfer coefficient
ε	Porosity
η	Overpotential

CL interface in their model by focusing on the impact of inhomogeneous compression. Though useful, these studies consider a lumped representation of the interface and neglected the true surface morphology of the DM and CL. Some literature has also focused on other interfaces like the bipolar plate (BP) and DM interface [15–18] by taking average morphology of the mating surface into consideration. Most of these studies focused on increase in ohmic resistance due to the contact. However, these interfacial gaps at MPL|CL may also act as a potential location for liquid water and can significantly affect the mass transport losses, or generate local heating from ohmic effects.

The objective of the present study is to obtain a better understanding of the impact of the true rough MPL|CL interface on the local ohmic, thermal and gas-phase mass transport losses. In the present work, a two-dimensional, single-phase, non-isothermal, anisotropic numerical model has been developed to investigate the impact of interfacial morphology on PEFC performance. Directly measured interfacial morphology information of a commercial catalyst layer and the micro-porous layer were experimentally characterized and integrated into a computational framework as a discrete interface layer, as discussed in the following section.

2. Model formulation

This section describes the two-dimensional, single-phase, non-isothermal model that incorporates the MPL|CL interfacial morphology information as a discrete domain. The model includes the transport of gaseous species, energy and charge. A schematic representation of the fuel cell components and the chosen control volume for the model development is shown in Fig. 1. Conservation
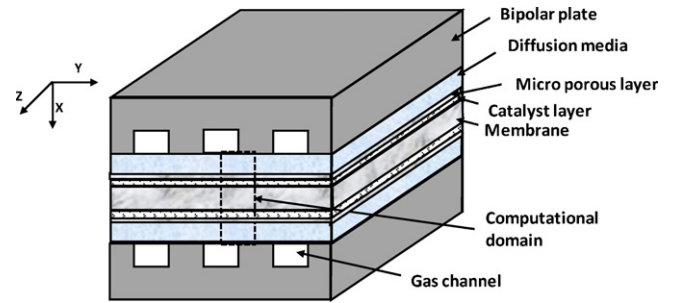

Fig. 1. Schematic representation illustrating the computational model domain.

of mass, energy and charge has been performed for each fuel cell component.

2.1. Model assumptions

In this study, a single-phase, non-isothermal, PEFC model was applied to typical fuel cell geometry with the interface layer on both the sides. The cell dimension and modeling parameters of the individual cell components are listed in Table 1, the properties of each component are summarized in Table 2, and various material properties are listed in Table 3. The following assumptions were made for the development of the single-phase PEFC model:

1. Model is two-dimensional (in x and y) as shown in Fig. 1 and has reached steady state.
2. MPL, DM and CL are considered to be porous media. The polymer electrolyte membrane (PEM) is treated with a pure diffusion model. Explicit treatment of liquid water motion is not accounted in porous media.
3. Conduction is assumed to be the dominant mode of heat transfer in the fuel cell components. Convective heat transfer due to flow of reactant gas species is neglected.
4. Thermo-osmotic flow in the membrane [20] is not included in the present formulation, as it would have negligible impact on the simulation performed here.
5. The MPL|CL interfacial structure [6] used in the present model is under homogeneous compression of 1.5 MPa.

2.2. Species transport

Species transport was derived for the reactant and product gases on the anode and cathode sides. A generalized form of Fick's law was used for the species transport. Species transport was solved for H_2 and H_2O on the anode side and O_2, N_2 and H_2O on the cathode side [19]:

$$D_i^{eff} \frac{\partial^2 C_i}{\partial x^2} + D_i^{eff} \frac{\partial^2 C_i}{\partial y^2} + S_i = 0 \tag{1}$$

where C_i is the molar concentration, D_i^{eff} is effective diffusion coefficient, and S_i is the source term for species. The first and second terms in Eq. (1) represent the through-plane (x-direction) diffusion and in-plane diffusion of reactant and product gases, respectively. The last term in Eq. (1) represents the consumption/production of the reactant species. This source term is non-zero in the catalyst layer and zero in other components. For H_2 and O_2, the source term in the catalyst layer can be written as:

$$S_i = -\frac{J_{gen}}{nF} \tag{2}$$

where n is the number of electrons transferred, J_{gen} is the local current density and F is Faraday's constant. For water, the first and second term in Eq. (1) represent diffusion and the source term in the

Table 1
Cell dimensions and modeling parameters.

Symbol	Parameter	Value	Unit
t_{DM}	Anode/cathode DM thickness	340	μm
t_{MPL}	Anode/cathode MPL thickness	80	μm
t_{CL}	Anode/cathode CL thickness	10 (Gore series MEA) [16]	μm
t_m	Membrane thickness	18 (Gore series MEA) [16]	μm
ε_{DM}	DM porosity	0.8	–
ε_{MPL}	MPL porosity	0.63 [28]	–
ε_{CL}	CL porosity	0.6	–
ε_{mc}	Volume fraction of ionomer in CL	0.26	–
$ai_{o,a}$	Exchange current density (anode)	10^9	$A\,m^{-3}$
$ai_{o,c}$	Exchange current density (cathode)	10^4	$A\,m^{-3}$
$D_{o,c}$	Diffusion coefficient of oxygen in cathode	3.2348×10^{-5}	$m^2\,s^{-1}$
$D_{o,a}$	Diffusion coefficient of hydrogen in anode	1.1028×10^{-4}	$m^2\,s^{-1}$
$D_{w,c}$	Diffusion coefficient of water vapor in cathode	7.35×10^{-5}	$m^2\,s^{-1}$
F	Faraday constant	96,487	$C\,(mol\text{-}eq)^{-1}$
R	Universal gas constant	8.314	$J\,(mol\,K)^{-1}$
$C_{H_2,ref}$	Reference hydrogen molar concentration	40	$mol\,m^{-3}$
$C_{O_2,ref}$	Reference oxygen molar concentration	40	$mol\,m^{-3}$
α_a	Anodic transfer coefficient for HOR	1	–
α_c	Cathodic transfer coefficient for HOR	1	–
α_c	Cathodic transfer coefficient for ORR	1	–
ΔS_a	Change in entropy for anode	0.104 [22]	$J\,(mol\,K)^{-1}$
ΔS_c	Change in entropy for cathode	−326.36 [22]	$J\,(mol\,K)^{-1}$

Table 2
Material properties values for fuel cell components.

Symbol	Property	DM	MPL	CL	PEM	Unit
σ_x	Through-plane electronic conductivity	300 [12]	300 [12]	200 [12]	–	$S\,m^{-1}$
σ_y	In-plane electronic conductivity	3000 [12]	300 [12]	200 [12]	–	$S\,m^{-1}$
k_x	Through-plane thermal conductivity	0.42 [23]	0.42 [23]	0.27 [23]	0.16 [23]	$W\,(mK)^{-1}$
k_y	In-plane thermal conductivity	4.2 [23]	4.2 [23]	2.7 [23]	0.16 [23]	$W\,(mK)^{-1}$

catalyst layer has an additional electro-osmotic drag term, which can be written as:

$$S_i = -\frac{J_{gen}}{nF} - \nabla \cdot \left(\frac{n_d}{F} i_e\right) \tag{3}$$

where n_d is electro-osmotic drag coefficient for water, and i_e is ionic current. Thermo-osmotic flow in the membrane [20] is not included in the present formulation. For the porous regions of a PEM fuel cell, diffusivity expression is modified to account for the tortuosity effect using Bruggman correlation as:

$$D_i^{eff} = \varepsilon^{1.5} D_i \tag{4}$$

where ε is the porosity of the medium.

2.3. Energy transport

For low to medium current, conduction is believed to be the dominant heat transfer mode in the porous fuel cell components [21]. To perform the energy conservation, advection heat transport

due to vapor diffusion and reactant/product species is neglected. Therefore, the generalized energy equation in two-dimension in all the PEFC components can be written as [21]:

$$k_x \frac{\partial^2 T}{\partial x^2} + k_y \frac{\partial^2 T}{\partial y^2} + S_{gen} = 0 \tag{5}$$

where T is the temperature, k_x and k_y is the thermal conductivity in x–y direction (anisotropic properties), and S_{gen} is the source term. The first and second term in Eq. (5) represents the through-plane and in-plane thermal transport, respectively. In the catalyst layer, the source term can be represented as:

$$S_{gen} = J_{gen}\left(\eta + \frac{T\,\Delta S}{nF}\right) + \frac{i_e^2}{\kappa} + \frac{i_s^2}{\sigma} \tag{6}$$

where η is overpotential, ΔS is entropy change, i_e is ionic current, i_s is electronic current, κ is ionic conductivity and σ is the electronic conductivity. These four terms represent irreversible heat of the electrochemical reaction, reversible entropic heat and Joule heating because of ionic current and electronic current respectively. In

Table 3
Material properties expressions.

Symbol	Property	Expression	Unit	Ref
κ	Ionic conductivity	$(0.5139\lambda - 0.326)\exp\left[1268\left(\frac{1}{303} - \frac{1}{T}\right)\right]$	$S\,m^{-1}$	[25]
n_d	Drag coefficient	$\frac{2.5\lambda}{22}$		[25]
λ	Water content	$\begin{cases} 0.043 + 17.81\alpha - 39.85\alpha^2 + 36.0\alpha^3, & 0 < a \leq 1 \\ 14 + 1.4(a-1) & \text{for } 1 < a \leq 3 \end{cases}$		
a	Water activity	$\frac{C_w RT}{P^{sat}}$		
P^{sat}	Saturation pressure	$\log_{10} P = -2.1794 + 0.02953(T - 273.15) - 9.1837 \times 10^{-5}(T - 273.15)^2 + 1.4454 \times 10^{-7}(T - 273.15)^3$	atm	
D_w	Diffusivity of water in membrane	$\begin{cases} 3.1 \times 10^{-7}\lambda(e^{0.28\lambda} - 1) \cdot e^{(-2346/T)}, & 0 < \lambda \leq 3 \\ 4.17 \times 10^{-8}\lambda(1 + 161e^{-\lambda}) \cdot e^{(-2346/T)} \end{cases}$	$m^2\,s^{-1}$	[24]
D_i	Diffusivity of species in gas phase	$D_o\left(\frac{T}{T_o}\right)^{3/2}\left(\frac{P_o}{P}\right)$	$m^2\,s^{-1}$	[29]

the membrane, the source term has Joule heating because of ionic current which can be represented as:

$$S_{gen} = \frac{i_e^2}{\kappa} \tag{7}$$

In micro-porous layer and diffusion media, the source term has Joule heating because of electronic current which can be represented as:

$$S_{gen} = \frac{i_s^2}{\sigma} \tag{8}$$

2.4. Charge transport

In the PEFC, protons travel through the ionic conductor (membrane and ionomer in the CL), while electrons transfer through the solid matrix (CL, MPL and DM). Conservation of charge is performed for both proton and electrons, and can be written as [19]:

$$\text{protons transport}: \quad \kappa_x \frac{\partial^2 \varphi_e}{\partial x^2} + \kappa_y \frac{\partial^2 \varphi_e}{\partial y^2} + J_{gen} = 0 \tag{9}$$

$$\text{electrons transport}: \quad \sigma_x \frac{\partial^2 \varphi_s}{\partial x^2} + \sigma_y \frac{\partial^2 \varphi_s}{\partial y^2} - J_{gen} = 0 \tag{10}$$

where φ_e and φ_s are the electrolyte and solid phase potentials, respectively. In both Eqs. (9) and (10), the first and second term represent through-plane and in-plane charge transport, respectively. All the material properties are considered as anisotropic in order to capture the effect of any gap due to the improper mating of MPL|CL. The source term in the charge equation is used to describe the transfer current between the electronic and electrolyte phase inside of each anode and cathode catalyst layer. In the anode catalyst layer, the kinetic expression represents the hydrogen oxidation reaction (HOR). The HOR kinetic expression is derived by linearizing the Butler–Volmer equation on the assumption that the HOR reaction is facile, and hence the surface overpotential is small. The local current density on anode side can be expressed as follows [19]:

$$\text{anode CL}: \quad J_{gen} = ai_{o,a}^{ref} \left(\frac{C_{H_2}}{C_{H_2,ref}} \right)^{1/2} \left(\frac{\alpha_a + \alpha_c}{RT} F\eta \right) \tag{11}$$

In the cathode catalyst layer, the kinetic expression represents the oxygen reduction reaction (ORR). The ORR kinetics can be represented by Tafel kinetics. The ORR kinetic expression is obtained by neglecting the oxidation branch of the Butler–Volmer equation for the cathode [19]:

$$\text{cathode CL}: \quad J_{gen} = -ai_{o,a}^{ref} \left(\frac{C_{O_2}}{C_{O_2,ref}} \right) \exp\left(-\frac{\alpha_c}{RT} F\eta \right) \tag{12}$$

For other components, the current generation source term is zero. The overpotential is defined as [30]:

$$\eta = \varphi_s - \varphi_e - U_{oc} \tag{13}$$

where U_{oc} is the open circuit potential, which is zero on anode side. The expression for cathode side can be derived from thermodynamics as:

$$U_{oc} = 1.23 - 9.0 \times 10^{-4}(T - 298.15) \tag{14}$$

As Nafion solution is used as the ionomer in the anode and cathode catalyst layers, the effective proton conductivity of the anode and the cathode catalyst layers is described using the Bruggman relation:

$$\kappa^{eff} = \varepsilon_{mc}^{1.5} \kappa \tag{15}$$

where ε_{mc} is the volume fraction of ionomer in the CL and κ is proton conductivity as a function of temperature and water content as shown in Table 3.
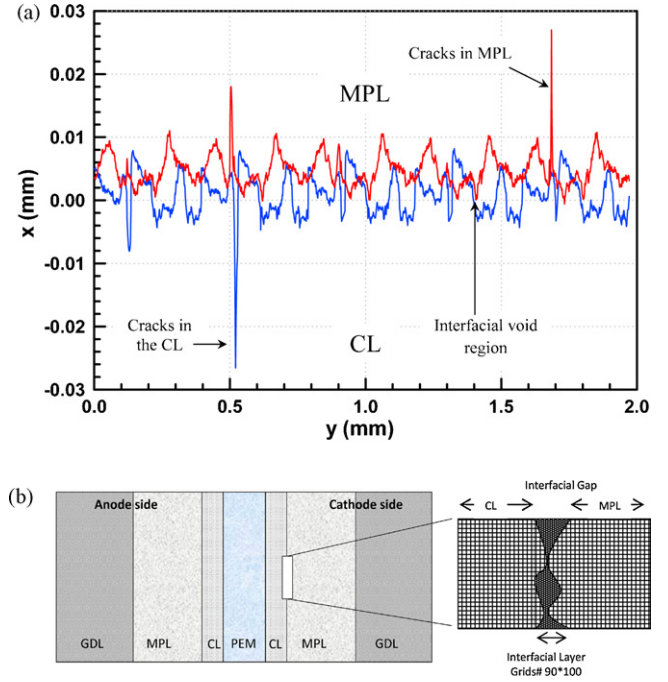

Fig. 2. (a) A typical MPL|CL interface cross-section based on the optical scans of MPL and CL surfaces [6]; (b) computational domain and interface layer.

2.5. Boundary conditions

The boundary conditions need to be specified in the through-plane direction (x-direction) only. Boundaries in other direction are symmetric; hence all gradients on these boundaries will be zero. By use of the single domain approach, the boundary conditions are only required at the external surfaces of the computational domain. At the anode/cathode channel inlet, the species concentrations are determined by the inlet pressure and humidity conditions. For the thermal boundary conditions, a constant temperature is applied to the anode and cathode land boundary. At the anode/cathode channel inlet, convective boundary conditions are applied for energy equation with Nusselt number calculated from internal laminar flow.

2.6. Treatment of interfacial layer

To investigate the effect of the interface between the cathode MPL|CL on PEFC performance, an additional layer consisting of MPL, CL surface and interfacial voids were included to the computational domain. A typical MPL|CL interface structure, which was constructed in our previous study [6], is shown in Fig. 2a. It must be noted that the horizontal axis and vertical axis in Fig. 2a correspond to the y axis and the x axis in the current formulation, respectively. Surfaces of CL and MPL (SGL 10BB) samples were characterized using optical profilometry to obtain the surface characteristics and profile data for digital reconstruction of the MPL|CL interface [5,6]. An interfacial morphological model was also developed at the Penn State FCDDL to obtain the resulting interface under compression [5,6]. It must be noted that the model approximates the deformation to be purely elastic. However, some plastic deformation in the contacting materials may occur, resulting in further compression of the MPL|CL interface under the pre-existing load. This would result in a relative reduction of the void size in the MPL|CL interface. Further studies are underway to account for the plastic deformation in the interfacial layer. This digitally reconstructed interface was incorporated in the present computational domain as shown in Fig. 2b. This interface layer consists of three parts:

Table 4
Interface layer properties.

Properties	Water vapor filled interface layer (Case 2)	Liquid water filled interface layer (Case 3)	Unit
Thermal conductivity	0.028	0.62	$W\,(mK)^{-1}$
Electronic conductivity	–	–	$S\,m^{-1}$
Oxygen diffusivity	3.23×10^{-5}	–	$m^2\,s^{-1}$
Hydrogen diffusivity	1.1×10^{-4}	–	$m^2\,s^{-1}$
Water vapor diffusivity	7.35×10^{-5} (anode) 1.1×10^{-4} (cathode)	7.35×10^{-5} (anode) 1.1×10^{-4} (cathode)	$m^2\,s^{-1}$

CL, MPL and void. Appropriate properties of each component were specified in each grid, depending on which region they were. The void region inside the interface layer is modeled as infinite resistivity for electron and proton transport, gas channel diffusivity of species transport and water vapor thermal conductivity for thermal transport. In a flooded scenario, this void space is filled by liquid water, and the appropriate thermal, mass and electric transport coefficients were specified in each grid. Fig. 2b summarizes the uniqueness of this model over other models published in the fuel cell literature, which is the incorporation of the MPL|CL interface layer with rough interfacial morphology.

2.7. Method of approach

The governing equations were discretized using a finite volume method and solved using a computational fluid dynamics code developed in-house. From a grid sensitivity study, computational mesh of 35,000 cells was found to provide sufficient special resolution. In the MPL and CL region, extremely finer meshes (90 in x-direction with 1 μm size and 100 in y-direction with 10 μm size) were used. An initial guess was given to all variables, and then scalar equations were solved to obtain the values of all the variables. Convergence criteria were performed for each variable and the procedure was repeated until convergence. Temperature-dependent properties and source term were updated each iteration. The coupled set of equations was solved iteratively, and the solution was considered to be convergent when relative error for each variable becomes less than 10^{-7}.

3. Results and discussion

To analyze the role of the interface layer on the PEFC performance, three cases have been defined for this study. In Case 1, the interface layer is not accounted for and a perfect contact is assumed. This is similar in nature to most existing performance model. In Cases 2 and 3, the interface layer consisting of the MPL, CL and interfacial voids is integrated into the computational domain. The precise morphology of this interface region was obtained from the experimental data for the CL and MPL [5,6] as previously discussed. Appropriate properties of each component are specified in each grid, depending on the appropriate region. The void region is assumed to be filled with water vapor for Case 2 and liquid water for Case 3. For both the cases, the interface layer is modeled as infinite resistivity for electron and proton transport. For Case 2, gas channel diffusivity for the species transport and water vapor thermal conductivity were used. Alternatively, Case 3 used a diffusivity value of almost zero for the reactant transport and liquid water thermal conductivity for thermal transport. Cases 2 and 3 are described in Table 4. These three cases have been simulated at different voltage boundary conditions (ranging from 0.4 to 1 V) to investigate their impacts on the mass, charge and energy transport.

The single-phase model with the interface layers was compared with measured experimental data [24]. The experimental data were obtained using Gore 5710 series MEA and SGL 10BB DM. The performance curve from the model results and the experimental results
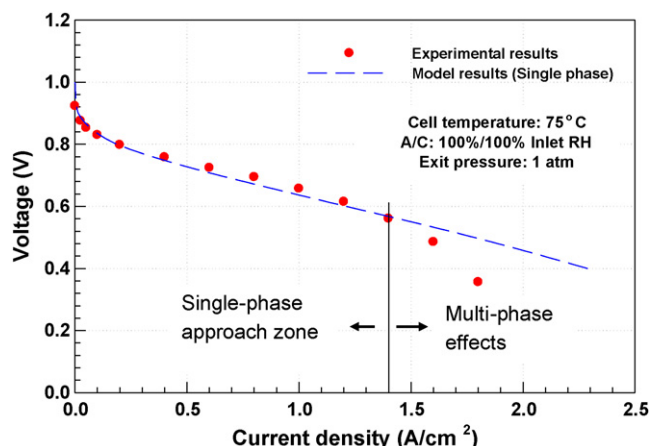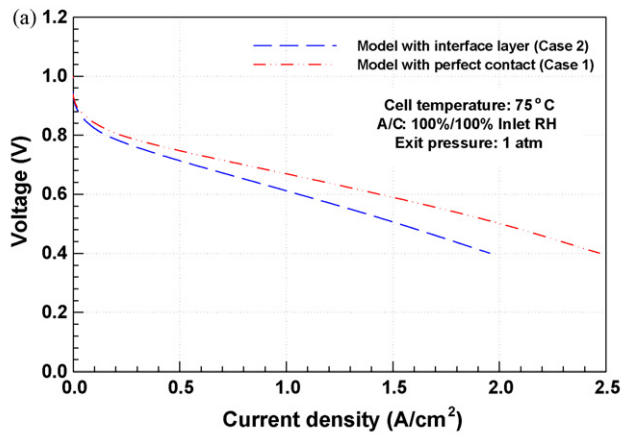

Fig. 3. Comparison of model results with experimental data [26] (Gore 5710 series MEA, SGL 10BB DM).

are shown in Fig. 3. The model results show reasonable agreement with the experimental data (~3% error) in the low current density region (less than $1.4\,A\,cm^{-2}$), considering the negligible effects of two-phase flow. For higher current densities (greater than $1.4\,A\,cm^{-2}$), the two-phase effects play important role, causing an increase in divergence between model results and experimental results.

3.1. Impact of water vapor filled interface layer

Fig. 4a shows the comparison between polarization curve for the Case 1 and Case 2. Case 1 has a perfect contact, and Case 2 has real interfacial layers with voids filled with water vapor. The polarization curve for both the cases were obtained by varying voltage from 1 to 0.4 V with step of 0.1 V. It can be seen that there is a decrease in the performance due to the addition of interface layers into the computational framework. In the activation region, the polarization curve for Case 2 is lower than Case 1, indicating more kinetic losses after the inclusion of interface in the model. This can be attributed to decrease in the CL volume due to voids present at the interface layer. The gap between PEFC performance curves increase with an increase in current density, indicating a potential increase in the ohmic losses for Case 2. Since the two phases are not taken into account, the model is valid only for lower current density region ($<1.4\,A\,cm^{-2}$). At $1\,A\,cm^{-2}$, additional voltage drop of ~54 mV is estimated for the Case 2 in comparison to Case 1. The individual anode overpotential, cathode overpotential and ohmic losses are shown for the Case 2 in Fig. 4b. Also, the additional individual losses and individual contributions are given. As the void region is filled with water vapor for Case 2, the major contribution of the losses comes from ohmic losses. The model predicts 68% ohmic contribution in overall additional voltage drop at $1\,A\,cm^{-2}$, which is ~37 mV. The ohmic loss increase for Case 2 can be attributed to an increased effective mean electron current flow path at the MPL|CL interface. The small impact on the anode overpotential and cathode overpotential is also seen in Fig. 4b. This can be attributed to the decrease in CL volume because of the voids present in the cata-

Fig. 4. (a) Polarization curve comparison of model with interface layer and model with perfect contact; (b) loss contributions at $1\,A\,cm^{-2}$ with inclusion of interface layer (water vapor filled).

| Losses	Voltage losses (Case 1) (mV)	Voltage losses (Case 2) (mV)	Additional losses (Case 2 − 1) (mV)	Individual contributions of additional losses
Ohmic Loss	63.3 ± 0.1	100.3 ± 0.1	36.9	68.1 %
Anode	12.9 ± 0.1	20.9 ± 0.1	7.9	14.6 %
Cathode	415.1 ± 0.1	424.5 ± 0.1	9.4	17.2 %
Over all losses	491.4 ± 0.1	545.7 ± 0.1	54.3	

Fig. 5. (a) Electron current distortion due to presence of the interface layer in complete PEFC domain; (b) detailed view of boxed region in (a).

lyst layer surface, which will affect the anode and cathode kinetics in PEFC. The model predicts 14.6% contribution of anode overpotential, and 17.2% contribution of cathode overpotential in overall additional voltage drop at $1\,A\,cm^{-2}$. These contributions depend on the current, and will change with different current. The ohmic contribution in additional voltage losses for Case 2 will increase for the current densities greater than $1\,A\,cm^{-2}$, and will decrease for current densities less than $1\,A\,cm^{-2}$.

For Case 1, the current moves from the diffusion media to the catalyst layer on the anode side, and from the catalyst layer to the diffusion media on the cathode side. After the inclusion of interface layer in the model for Case 2, there is void region present in MPL|CL interface. This void region acts as an electrical insulation barrier for the charge transport, which results in the significant in-plane current flow. The additional ohmic voltage loss is attributed to the in-plane motion of electron due to the void region present at the interface layer, which causes current distortion shown in Fig. 5. Fig. 5a shows the electron current vector plot of the complete PEFC domain for Case 2 at $1\,A\,cm^{-2}$. Fig. 5b shows the detailed view of boxed region in Fig. 5a. It can be seen from the figure that there exists significant in-plane motion of electron current in the catalyst layer, micro-porous layer and diffusion media.

3.2. Impact of anisotropicity

In-plane conductivity of the micro-porous and catalyst layer is expected to be the critical parameter for controlling the additional voltage loss for Case 2. Fig. 6 shows the variation of the overall additional losses at $1\,A\,cm^{-2}$ for Case 2 with an increase in the in-plane conductivity. The x axis shows the multiplying factor used to increase the in-plane conductivity of the MPL and the CL. As the in-plane conductivity increases, there is a decrease in overall losses predicted by the model. Fig. 6 also shows that the additional voltage loss for Case 2 asymptotically approaches to ~17 mV value, which is the same as the additional anode/cathode overpotential losses
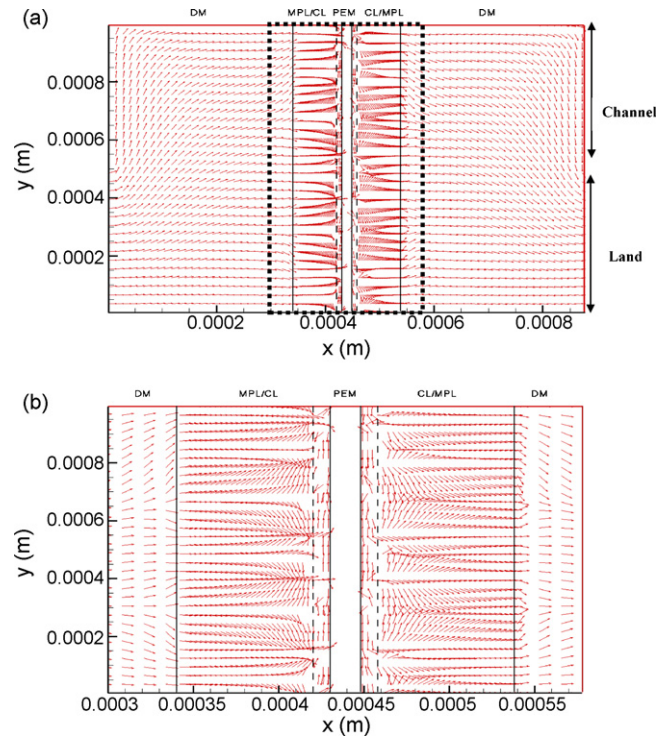
for Case 2. This means that the additional ohmic losses for Case 2 can be removed by increasing the in-plane conductivity of the micro-porous layer and catalyst layer. Fig. 5b shows significant in-plane motion of electron current in the diffusion media as well. But the in-plane conductivity of the diffusion media is 8–10 times the in-plane conductivity of the catalyst layer and micro-porous layer. Therefore, the impact on overall additional loss is almost negligible.

3.3. Temperature distribution

Fig. 7 shows the temperature distribution of PEFC for Case 2 at $1\,A\,cm^{-2}$. It can be seen that the temperature at the cathode side is higher than at the anode side, due to the reversible and irreversible entropy production. Also it can be seen for Case 2 in Fig. 7
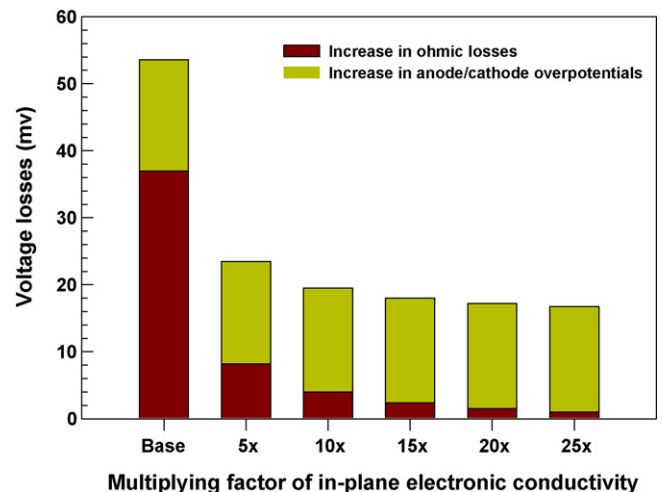
Fig. 6. Impact of CL and MPL in-plane conductivity on overall losses caused by inclusion of interface layer.
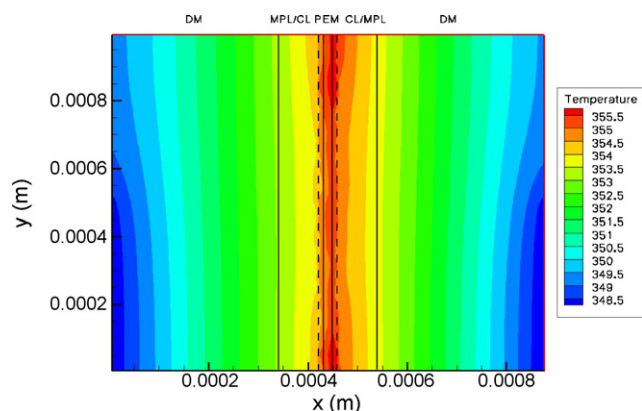
Fig. 7. Temperature distribution inside PEFC (water vapor filled interface layer).

Fig. 9. (a) Performance comparisons with liquid water filled interfacial layer; (b) loss contributions at $1\,A\,cm^{-2}$ because of inclusion of interface layer (liquid water filled) and comparison of individual contribution with water vapor filled and liquid water filled interface layer at $1\,A\,cm^{-2}$.

that there are some hot spots formed close to the contact points between MPL|CL interface on the cathode side. A maximum temperature difference of $1\,°C$ is observed on the cathode CL. Reaction region in cathode CL close to the contact points at MPL|CL interface will be more active than reaction region just behind the voids present at the interface. This may cause more heat generation due to the reaction close to the contact points. Also there is high amount of charge flow at the contact points at the MPL|CL interface. Temperature variation in cathode CL may also be attributed to the heat generation due to Joule heating of large amount of charge flowing at the contact points.

Fig. 8a and b shows the temperature distribution of the anode and the cathode interface layer region of PEFC for Case 2 at $1\,A\,cm^{-2}$. Fig. 8a includes the Joule heating effects due to electron flow and Fig. 8b does not include the Joule heating effects due to electron flow. It can be seen that there is an increase of ∼$0.3\,°C$ temperature with the inclusion of the Joule heating due to the electron flow close to the contact points at MPL|CL interface. This is attributed to the large amount of charge flowing at the contact points. This temperature rise has very small impact on the performance (0.02% change in output voltages) in the single-phase model. It can be concluded that temperature variation of $1\,°C$ in cathode CL region is mainly caused by voids present at the interface layer and only a small impact from the electron flow at the contact points between the CL and the MPL.
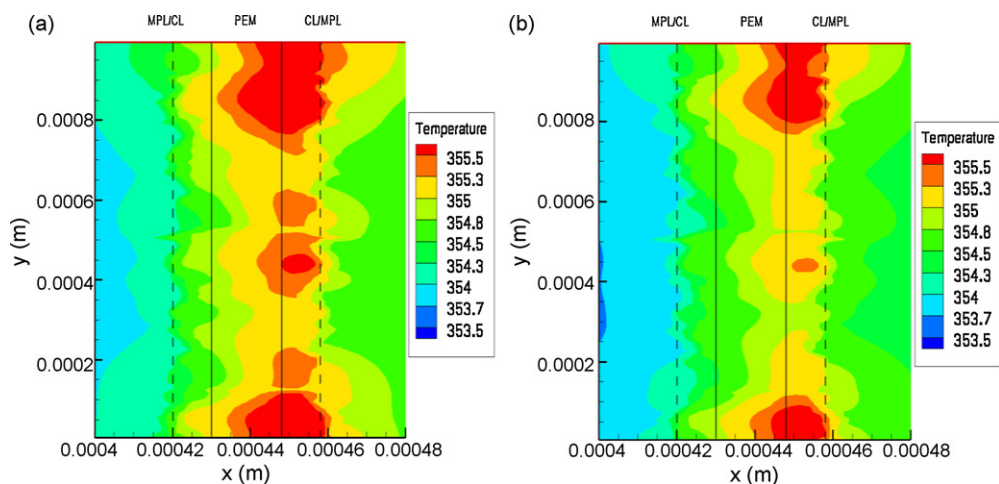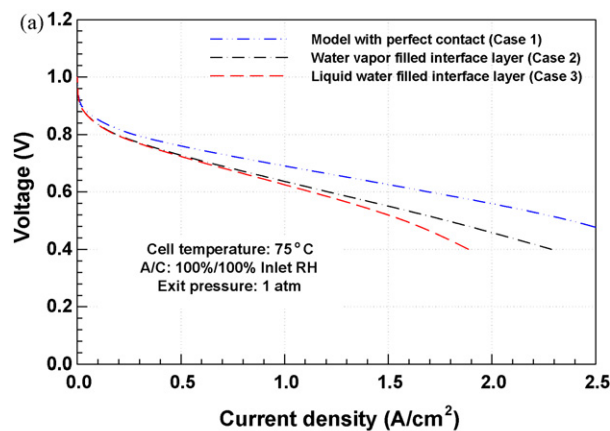
3.4. Impact of liquid water pooling at interfacial voids

Fig. 9a shows the comparison between polarization curve for the Case 1 and the Case 3. Case 1 has no interface layer and Case 3 has interface layer with voids filled with liquid water. As described, the polarization curves for both the case are obtained by changing voltage from 1 to 0.4 V. Similar to Fig. 4, there is a decrease in performance after the inclusion of liquid water filled interface layer in to the model. For low current densities, the polarization curve for Case 3 is overlapping with polarization curve of Case 2. It can be concluded that kinetic loss are same for Case 2 and Case 3, and higher than Case 1, due to the void present in catalyst layer. But at high current densities where the mass transport losses become more important, the polarization curve for Case 3 is predicted to be lower than polarization curve of Case 2. This behavior is attributed

Fig. 8. (a) Temperature distribution with electron transport Joule heating; (b) temperature distribution without electron transport Joule heating.
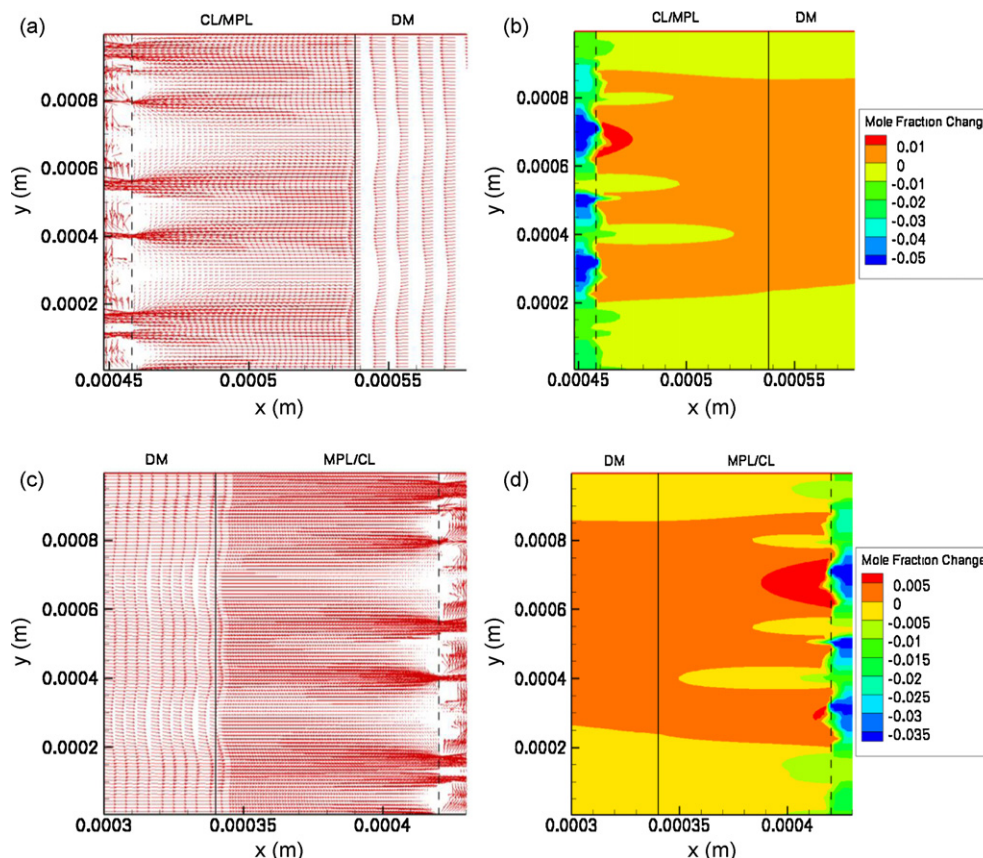
Fig. 10. (a) Anode side hydrogen diffusion vector distortions caused by liquid water filled interface layer; (b) mole fraction change of hydrogen between Case 3 and Case 1; (c) cathode side oxygen diffusion vector distortions caused by liquid water filled interface layer; (d) mole fraction change of oxygen between Case 3 and Case 1.

to the blockage of species transport because of the liquid accumulation at the interface layer. At $1\,A\,cm^{-2}$, an additional voltage drop of ~66 mV is estimated for the Case 3 in comparison to Case 1. Fig. 9b shows the individual anode overpotential, cathode overpotential and ohmic losses for Case 3 at $1\,A\,cm^{-2}$. The increase in individual voltage losses is calculated for Case 3 in comparison to Case 1. The model predicts ~34 mV of increase in ohmic loss, ~8 mV of increase in anode overpotential and ~25 mV of increase in cathode overpotential. The highest contribution comes from ohmic losses (51%) in additional voltage loss of Case 3 in comparison to Case 1. This is followed by cathode overpotential (37%) and anode overpotential (12%). Fig. 9b also shows the comparison between the additional individual voltage losses at $1\,A\,cm^{-2}$ for Cases 2 and 3 in comparison to Case 1. It can be seen that Case 3 has more additional overall losses in comparison to Case 2. This can be attributed to additional mass transport losses in Case 3. Therefore as current increases, voltage loss between Case 2 and 3 increases. Because of liquid water accumulation at the interface, reaction rates adjacent to liquid water filled gaps are slower in comparison to other region in the catalyst layer. This leads to a decrease in in-plane motion of electron current for Case 3 which causes 8.5% decrease in additional ohmic loss in comparison to Case 2. As hydrogen diffusivity and mole fraction on the anode side is very high in comparison to oxygen, negligible increase (0.2%) is seen on the anode overpotential. Alternatively, significant jump (162.8% increase) in cathode overpotential is observed for Case 3 in comparison to Case 2. This is attributed to the blockage of oxygen transport on the cathode side of PEFC.

As discussed in previous paragraph, a negligible increase in anode overpotential and a significant increase in cathode overpotential are predicted by the model for Case 3 in comparison to Case

2. This is due to the mass transport losses caused by the liquid water filled interface layer on both the sides of the model. Fig. 10 shows the disruptions in species transport caused by the liquid water filled interface layer on the anode and cathode side of the model. Liquid water blocks the diffusion of species transport causing a decreasing in mole fraction of species in reaction sites. A diffusion vector plot shows the disruptions caused by the interface layer for the hydrogen transport on the anode side and for the oxygen transport on the cathode side. The change in mole fraction of species of Case 3 in comparison to Case 1 is shown in contour plot in Fig. 10. A maximum decrease of 0.035 mole fraction of hydrogen is estimated adjacent to liquid filled gaps on the catalyst layer with slight increase (0.005 mole fraction) on the diffusion media and microporous layer. Similar behavior is observed for oxygen transport on the cathode side for which maximum decrease of 0.05 mole fraction is estimated on the catalyst layer with slight increase (0.01 mole fraction) on diffusion media and micro-porous layer. Higher impact on oxygen mole fraction is attributed to the low diffusivity of oxygen in comparison to hydrogen.

3.5. Effects of interfacial gap width and location

Separate cases are simulated to know the impact of interfacial gap width and location on the PEFC performance. At $0.5\,A\,cm^{-2}$, Fig. 11 shows the variation of additional voltage losses with the increase in width of gap at MPL|CL interface. An interfacial gap is placed in between MPL and CL at the center of channel on the cathode side of PEFC. Additional voltage loss is plotted with a non-dimensional parameter defined as gap width, W/δ (W is the interfacial gap width and δ is the catalyst layer thickness). The parameter W/δ, is defined because the catalyst layer resistance
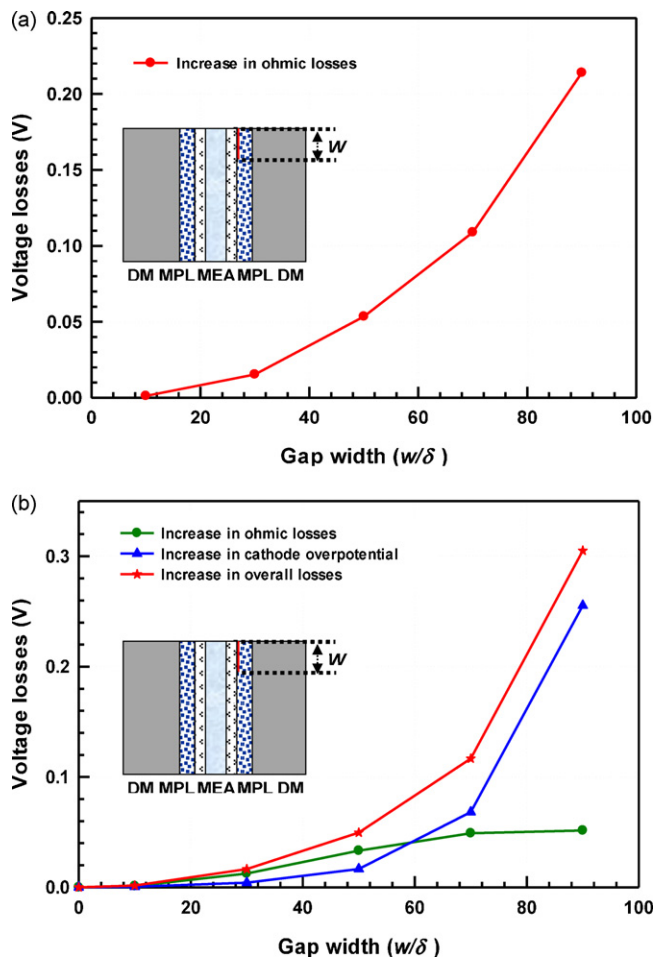
Fig. 11. (a) Increase in ohmic losses due to increase in interfacial gap width. Gap assumed to be filled with water vapor; (b) gap assumed to be filled with liquid water at 1 A cm^{-2}.
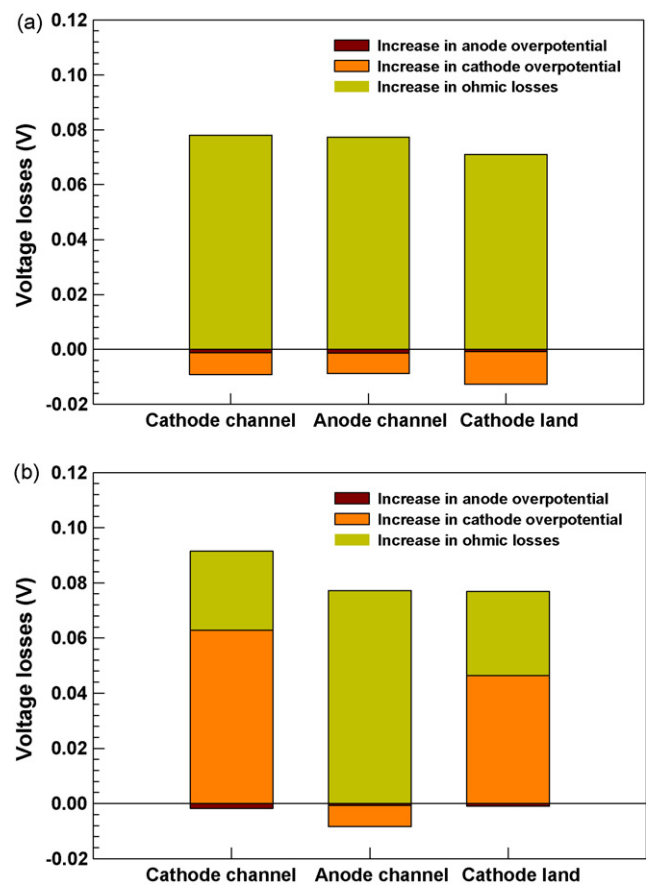
Fig. 12. (a) Voltage losses at different locations of gap with $W/\delta = 50$ (water vapor filled); (b) voltage losses at different locations of gap with $W/\delta = 50$ (liquid water filled) at 1 A cm^{-2}.

is a key parameter for overall MPL|CL interfacial resistance [27]. For Fig. 11a, the gap region is assumed to be filled with water vapor. It is modeled as infinite resistivity for electron and proton transport. Gas channel diffusivity is used for species transport and water vapor thermal conductivity is used for thermal transport. For this case, additional ohmic losses are found to be dominant. The model results predict that as the width of gap increases, additional ohmic losses increases in a non-linear fashion. The additional ohmic loss increase is attributed to an electrical insulation barrier due to the interfacial gap, which causes voltage and current distortion. It is also observed that there is no increase in additional ohmic loss till $W/\delta = 10$, which is critical gap width after which additional ohmic losses start playing role. Alternatively, the gap region is assumed to be filled with liquid water for Fig. 11b. It is modeled as infinite resistivity for electron and proton transport. Almost zero diffusivity is used for species transport and liquid water thermal conductivity is used. For this case, significant effects are seen on the additional ohmic losses and additional cathode overpotentials. Fig. 11b shows the variation of additional overall losses, additional cathode overpotential and additional ohmic losses with the increase in gap width. As the gap width increases, both the additional cathode overpotential and additional ohmic losses increases resulting in the increase of additional overall losses. The increase in additional cathode overpotential is attributed to the blockage of oxygen transport because of water filled gaps. Fig. 11b shows less impact on additional ohmic losses in comparison to Fig. 11a. This may be attributed to the decrease in in-plane

motion of electron because of slower reaction rates adjacent to the liquid water filled gaps. As current density increases, there will be increase in the additional overall losses and individual contributions.

At 1 A cm^{-2}, the individual contributions of the additional anode overpotential, cathode overpotential and ohmic losses at three different locations of gap are shown in Fig. 12. The interfacial gap of dimensionless width parameter of 50 is placed at the cathode channel center, anode channel center and cathode land center. Fig. 12a shows the loss when the gap is filled with water vapor. The model prediction shows that the additional overall losses are dominated by the additional ohmic losses. With the change in the location of gap, no significant change is predicted in the losses and individual contributions. Alternatively, significant changes are predicted with the location when the gap is filled with liquid water as shown in Fig. 12b. A gap located at cathode channel center is found to be most critical for performance loss followed by gap located at the cathode land center and anode channel center. Model predictions show that the increase in cathode overpotential contribution is dominating in increase in overall losses when the liquid filled gap is located at the cathode side of PEFC. This can be attributed to the blockage in oxygen transport caused by liquid water filled gap. There is a blockage of hydrogen transport on anode side of PEFC when the gap is located at the anode channel center, but no significant impact is seen on anode/cathode overpotentials. This can be attributed to high diffusivity values and high mole fraction of hydrogen on the anode side. Therefore, the individual additional losses for liquid water filled gap are almost same as the water vapor filled gap.

4. Summary and conclusions

A mathematical model was developed to investigate the effect of true interfacial morphology on fuel cell performance. The novel feature of the model is the inclusion of directly measured surface morphological information of the catalyst layer and the microporous layer, and inclusion of interfacial voids present in CL|MPL interface. The conclusions can be drawn from this analysis includes:

- Model predictions show a decrease in the performance curve of the PEFC with presence of interface layer. In case of water vapor filled voids in the interface layer, ohmic losses are significant (~68% contribution) as compared to cathode and anode overpotentials. However, cathode overpotential (increase of ~25 mV) becomes significant if liquid water is pooled in these interfacial pores.
- In-plane conductivity of the components adjacent to interface layer is found to be the key controlling parameter for additional ohmic loss caused by the inclusion of interface layers. A decrease of 30.06 mV in performance loss is found by increasing the in-plane conductivity by 5 times.
- Temperature variation (~1 °C) is found close to the contact points of the MPL|CL interface mainly because of the low active region formation in CL behind the voids present at the interface layer, but are not shown to affect overall performance.
- A dimensionless width of 10 is critical water vapor filled gap width after which ohmic losses become significant. The maximum impact is caused at the cathode channel center liquid filled gap followed by the anode channel center and cathode land center for the simulated fuel cell in this model.

Acknowledgements

References

[1] T.A. Zawodzinski, C. Derouin, S. Radzinski, R.J. Sherman, V.T. Smith, T.E. Springer, S. Gottesfeld, J. Electrochem. Soc. 140 (1993) 1041–1047.
[2] T.A. Zawodzinski, T.E. Springer, J. Davey, R. Jestel, C. Lopez, J. Valerio, S. Gottesfeld, J. Electrochem. Soc. 140 (1993) 1981–1985.
[3] M.L. Perry, T.F. Fuller, J. Electrochem. Soc. 149 (2002) S59–S67.
[4] K.B. Prater, J. Power Sources 51 (1994) 129–144.
[5] F.E. Hizir, S.O. Ural, E.C. Kumbur, M.M. Mench, J. Power Sources, 2010, doi:10.1016/j.jpowsour.2009.11.032.
[6] T. Swamy, E.C. Kumbur, M.M. Mench, J. Electrochem. Soc. 157 (2009) B77–B85.
[7] H. Bajpai, M. Khandelwal, E.C. Kumbur, M.M. Mench, ECS Trans. 25 (2009) 3–13.
[8] T. Swamy, F.E. Hizir, M. Khandelwal, E.C. Kumbur, M.M. Mench, ECS Trans. 25 (2009) 15–27.
[9] C. Hartnig, I. Manke, R. Kuhn, N. Kardjilov, J. Banhart, W. Lehnert, Appl. Phys. Lett. 92 (2008) 1–3, 134106.
[10] S. Kim, M.M. Mench, J. Power Sources 174 (2007) 206–220.
[11] S. Kim, B.K. Ahn, M.M. Mench, J. Power Sources 179 (2008) 140–146.
[12] S. Kim, M. Khandelwal, C. Chacko, M.M. Mench, J. Electrochem. Soc. 156 (2009) B99–B108.
[13] T. Hottinen, O. Himanen, S. Karvonen, I. Nitta, J. Power Sources 171 (2007) 113–121.
[14] I. Nitta, S. Karvonen, O. Himanen, M. Mikkola, Fuel Cells 8 (2008) 410–421.
[15] X. Lai, D. Liu, L, Peng, J. Ni, J. Power Sources 182 (2008) 153–159.
[16] L. Zhang, Y. Liu, H. Song, S. Wang, Y. Zhou, S.J. Hu, J. Power Sources 162 (2006) 1165–1171.
[17] Y. Zhou, G. Lin, A.J. Shih, S.J. Hu, J. Power Sources 163 (2007) 777–783.
[18] Z. Wu, S. Wang, L. Zhang, S.J. Hu, J. Power Sources 189 (2006) 1066–1073.
[19] M.M. Mench, Fuel Cell Engines, John Wiley & Sons, New York, 2008.
[20] S. Kim, M.M. Mench, J. Membr. Sci. 328 (2009) 113–120.
[21] D. Poulikakos, Conduction Heat Transfer, Englewood Cliff, 1994.
[22] M.J. Lampinen, M. Fomino, J. Electrochem. Soc. 140 (1993) 3537–3546.
[23] M. Khandelwal, M.M. Mench, J. Power Sources 161 (2006) 1106–1115.
[24] S. Motupally, A.J. Becker, J.W. Weidner, J. Electrochem. Soc. 147 (2000) 3171–3177.
[25] T.E. Springer, M.S. Wilson, S. Gottesfeld, J. Electrochem. Soc. 140 (1993) 3513–3526.
[26] M.P. Manahan, S. Kim, E.C. Kumbur, M.M. Mench, ECS Trans. 25 (2009) 1745–1754.
[27] C. Chacko, R. Ramasamy, S. Kim, M. Khandelwal, M.M. Mench, J. Electrochem. Soc. 155 (2008) B1145–B1154.
[28] K.T. Cho, M.M. Mench, Measurements by The Pennsylvania State University, Fuel Cell Dynamics and Diagnostics Laboratory.
[29] R.B. Bird, W.E. Stewart, E.N. Lightfoot, Transport Phenomena, John Wiley & Sons, New York, 2002.
[30] A.J. Bard, L.R. Faulkner, Electrochemical Methods Fundamentals and Applications, John Wiley & Sons, New York, 2001.